Thermodynamic Model and Database for Sulfides Dissolved in Molten Oxide Slags

YOUN-BAE KANG and ARTHUR D. PELTON

A thermodynamic model has been developed in the framework of the modified quasichemical model in the quadruplet approximation to permit the calculation of solubilities of various gaseous species (sulfide, sulfate, nitride, carbide, water, *etc.*) in molten slags. The model calculates the solubilities solely from knowledge of the thermodynamic activities of the component oxides and the Gibbs energies of the pure liquid components (oxides, sulfides, sulfates, *etc.*). In the current article, it is shown that solubilities of sulfur as sulfide in Al_2O_3-CaO-FeO-Fe_2O_3-MgO-MnO-SiO_2-TiO_2-Ti_2O_3 multicomponent slags, which are predicted from the current model with no adjustable model parameters, are in good agreement with all available experimental data. The article also provides a thorough review of experimental sulfide capacity data for this system. The model applies at all compositions from pure oxides to pure sulfides and from basic to acidic slags. By coupling this database with other evaluated databases, such as those for molten metal and gaseous phases, and with general software for Gibbs energy minimization, practically important slag/metal/gas/solid equilibria can be computed such as S-distribution ratios.

DOI: 10.1007/s11663-009-9283-6

I. INTRODUCTION

VARIOUS gaseous species like S, N, C, and H dissolve in molten oxide slags as sulfide, sulfate, nitride, carbide, carbonate, and so on. Knowledge of the solubility of these gaseous species in slags is important. For example, control of the sulfur level in many grades of commercial products, such as steel, copper, and lead, can be achieved by control of the distribution ratio of sulfur between the liquid metals and the molten slags. In steel, a low sulfur content is usually desired because of the detrimental effect of sulfur on many types of final products. However, relatively high sulfur content is desired in some steel grades, such as fast-cutting steels.

Approaches have been proposed to correlate the sulfide solubility with the optical basicity[1] or bulk composition[2] of slags. These approaches generally require several empirical model parameters; that is, they have low predictive ability. A more fundamental approach was proposed by Gaye and Lehmann,[3] who included sulfide solubility in the IRSID cell model. This approach has been more successful but still requires several empirical parameters.

In the model of Reddy and Blander,[4] which was later modified by Pelton *et al.*,[5] the activity of sulfide in the slag is calculated from considerations of its configurational entropy of mixing with the silicate structural units, whereas the activities of the oxide components of the slag are taken from existing evaluated databases. This model yields good predictions of sulfide solubility in multicomponent slags, with no adjustable model parameters. The model has been extended[6] with equal success to the dissolution of other species (SO_4^{2-}, CO_3^{2-}, I^-, *etc.*).

In the current article, we report on a new model for the solubility of gaseous species in molten slags within the framework of the modified quasichemical model (MQM) in the quadruplet approximation.[7] This model is similar to the Reddy–Blander–Pelton (RBP) model inasmuch as the sulfide activities are calculated from considerations of the configurational entropy of structural units, whereas the oxide activities are taken from existing extensive evaluated thermodynamic databases, which we have developed during the last 30 years. Like the RBP model, the model involves no adjustable empirical parameters. It is superior to the RBP model inasmuch as it applies even in highly acidic slags and even at high sulfide contents, and its predictive ability is generally even better. The model has been incorporated into the FactSage[8,9] databases and software (Therm-Fact Ltd., Montreal, Canada and GTT-Technologies, Herzogenrath, Germany).

Sulfide solubilities calculated from the model are compared with all available data for the molten slag system Al_2O_3-CaO-FeO-Fe_2O_3-MgO-MnO-SiO_2-TiO_2-Ti_2O_3. The current article also provides a thorough review of sulfide capacity measurements in this system.

II. THERMODYNAMIC MODEL

It is assumed that the molten oxide-containing sulfur consists of the following two sublattices: (Ca^{2+}, Mg^{2+}, Si^{4+}, Al^{3+}, …)[O^{2-}, S^{2-}]. Cations such as Ca^{2+}, Mg^{2+},

YOUN-BAE KANG, Research Associate, and ARTHUR D. PELTON, Professor and Co-director, are with the Centre de Recherche en Calcul Thermochimique (CRCT), Département de Génie Chimique, École Polytechnique, P.O. Box 6079, Station "Downtown," Montréal, Quebec, Canada H3C 3A7. Contact e-mail: youn-bae.kang@polymtl.ca, arthur.pelton@polymtl.ca.

Manuscript submitted February 13, 2009.
Article published online August 25, 2009.

Si^{4+}, and Al^{3+} reside exclusively on the cationic sublattice, whereas anions such as O^{2-} and S^{2-} reside exclusively on the anionic sublattice.

Consider a $CaO\text{-}SiO_2$ slag containing S. In Figure 1, a schematic composition square is shown for this "reciprocal" ionic system. The following two reactions must be considered in the model. The first is the exchange reaction among the pure liquid components:

$$2CaO(l) + SiS_2(l) = 2CaS(l) + SiO_2(l) \quad \Delta g^{\text{exchange}}_{\text{CaSi/OS}} \quad [1]$$

If $\Delta g^{\text{exchange}}_{\text{CaSi/OS}}$ is negative, then reaction[1] is displaced to the right. This equilibrium determines the first-nearest-neighbor (FNN) cation-anion short-range-ordering (SRO) in the slag. Because $\Delta g^{\text{exchange}}_{\text{CaSi/OS}}$ is of the order of −400 kJ/mol, the FNN SRO is extremely strong, with Ca-S and Si-O FNN pairs being strongly favored over Ca-O and Si-S pairs.

Second, it is well known that molten oxides often show strong second-nearest-neighbor (SNN) SRO between cations. For example, in $CaO\text{-}SiO_2$ slags, the maximum SNN SRO occurs near the Ca_2SiO_4 composition where nearly all Si^{4+} cations have Ca^{2+} cations in their second coordination shell (equivalent to a model of Ca^{2+} cations and SiO_4^{4-} orthosilicate anions). This is taken into account by the following SNN pair exchange reaction:

$$(\text{Ca-O-Ca}) + (\text{Si-O-Si}) = 2(\text{Ca-O-Si}); \quad \Delta g_{\text{CaSi/OO}} \quad [2]$$

For many molten oxide systems, the Gibbs energy changes of these SNN pair exchange reactions are negative (*e.g.*, $\Delta g_{\text{CaSi/OO}} \sim -60$ kJ/mol) and SNN SRO is consequently important.

For the reciprocal system in Figure 1, there are three other SNN pair exchange reactions, such as the pair exchange reaction between O^{2-} and S^{2-} in the presence of Ca^{2+}:

$$(\text{S-Ca-S}) + (\text{O-Ca-O}) = 2(\text{S-Ca-O}); \quad \Delta g_{\text{CaCa/OS}} \quad [3]$$

As will be shown later, it may be assumed that the Gibbs energy changes of these three reactions are relatively small.

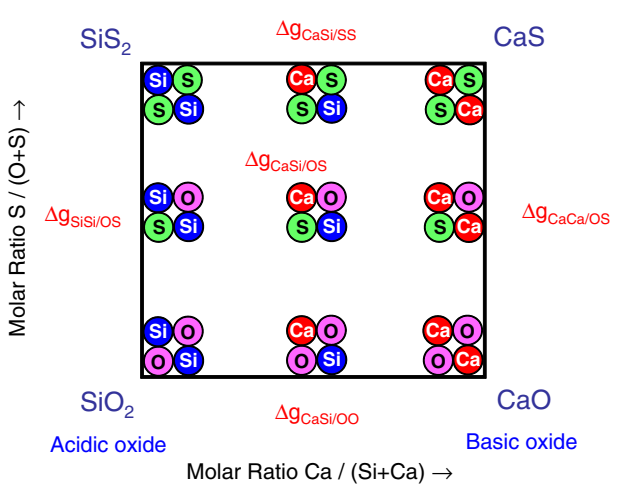

Fig. 1—The nine quadruplets in $CaO\text{-}SiO_2\text{-}CaS\text{-}SiS_2$ melts.

Finally, the coupling of the FNN SRO and SNN SRO must be taken into account in the thermodynamic modeling. To model the Gibbs energy of two-sublattice reciprocal ionic liquids with simultaneous FNN and SNN SRO, an MQM in the quadruplet approximation was developed by Pelton *et al.*[7] and has been successfully applied to many molten salt systems.[10–13] In applying this model to $CaO\text{-}SiO_2\text{-}CaS\text{-}SiS_2$ slags, nine quadruplet "clusters" are defined as shown in Figure 1, where each quadruplet consisted of two cations and two anions. These quadruplets are distributed randomly over "quadruplet" sites. Hence, the SNN pairs shown in reaction[2] are associated with the quadruplets CaCa/OO, SiSi/OO, and CaSi/OO. A complete mathematical description of the model is given by Pelton *et al.*[7]

The Gibbs energy of the solution is given by

$$\begin{aligned} G = {} & (n_{\text{CaCa/OO}} g_{\text{CaCa/OO}} + n_{\text{SiSi/OO}} g_{\text{SiSi/OO}} \\ & + n_{\text{CaCa/SS}} g_{\text{CaCa/SS}} + n_{\text{SiSi/SS}} g_{\text{SiSi/SS}}) \\ & + (n_{\text{CaSi/OO}} g_{\text{CaSi/OO}} + n_{\text{CaSi/SS}} g_{\text{CaSi/SS}} \\ & + n_{\text{CaCa/OS}} g_{\text{CaCa/OS}} + n_{\text{SiSi/OS}} g_{\text{SiSi/OS}}) \\ & + (n_{\text{CaSi/OS}} g_{\text{CaSi/OS}}) - T\Delta S^{\text{config}} \end{aligned} \quad [4]$$

where $n_{ij/kl}$ and $g_{ij/kl}$ are the number of moles and the molar Gibbs energy of the ij/kl quadruplets and ΔS^{config} is the configurational entropy of mixing that is given by randomly distributing the quadruplets over the sublattices, taking into account the fact that anion-cation pairs are shared among quadruplets. Because the exact mathematical expression for such a distribution is not known, the configurational entropy is approximated by a cluster-variational equation as given in Reference 7.

The model requires FNN and SNN coordination numbers for each ion. In our previous modeling of oxide slags, during the development of our oxide slag database, appropriate SNN coordination numbers were assigned to all cations and to O^{2-}. Although the general model permits coordination numbers to vary with composition, this complexity was not required in the current oxide slag database and is not required in the current study. That is, the coordination number of a given ion is the same at all compositions. (In the notation of Reference 7: $Z^i_{ii/\text{OO}} = Z^i_{ij/\text{OO}}$ for all i and j.) In the current study, we assume that the cation coordination numbers are the same in mixed oxide/sulfide solutions as in oxide solutions and that the coordination number of S^{2-} is the same as that of O^{2-}. Finally, we make the simplifying assumption that all FNN coordination numbers z_i are equal to twice the corresponding SNN coordination numbers Z_i. (In the notation of Reference 7, this is equivalent to setting $\zeta = 1$.)

In Eq. [4], the Gibbs energies $g_{ii/\text{OO}}$ and $g_{ii/\text{SS}}$ of the unary quadruplets at the four corners of Figure 1 are given by the Gibbs energies of the pure liquid oxides and sulfides. For example:

$$g_{\text{CaCa/OO}} = \left(\frac{2}{Z_{\text{Ca}}}\right) g^{\circ}_{\text{CaO}} \quad [5]$$

where Z_{Ca} is the SNN coordination number of Ca^{2+} and g°_{CaO} is the standard molar Gibbs energy of pure liquid CaO. For details, see Reference 7.

The Gibbs energies of the binary quadruplets in Eq. [4] ($g_{CaSi/OO}$, $g_{CaSi/SS}$, $g_{CaCa/OS}$, and $g_{SiSi/OS}$) on the four edges of Figure 1 are given from the Gibbs energies of the SNN pair exchange reactions. For example, Eq. [2] for the SNN pair exchange reaction in the CaO-SiO_2 binary system is equivalent to the following reaction among quadruplets:

$$(CaCa/OO)_{quad} + (SiSi/OO)_{quad} = 2(CaSi/OO)_{quad}; \quad \Delta g_{CaSi/OO} \qquad [6]$$

Hence,

$$2g_{CaSi/OO} = g_{CaCa/OO} + g_{SiSi/OO} + \Delta g_{CaSi/OO} \qquad [7]$$

where $\Delta g_{CaSi/OO}$ is a model parameter for the CaO-SiO_2 system, which can be a function of temperature and composition. This parameter is known from our previous evaluation/optimization of all experimental and phase equilibrium data in this binary system.[14] Similarly, all other SNN oxide pair exchange energies $\Delta g_{ij/OO}$ (where i, j = Al^{3+}, Ca^{2+}, Fe^{2+}, Fe^{3+}, Mg^{2+}, Mn^{2+}, Si^{4+}, Ti^{3+}, Ti^{4+}) have been previously evaluated and optimized and stored in our database for oxide slags.[14–30]

The other three SNN pair exchange energies, $\Delta g_{CaSi/SS}$, $\Delta g_{CaCa/OS}$, and $\Delta g_{SiSi/OS}$, on the other three edges of Figure 1 are assumed to be zero. This is equivalent to assuming ideal mixing behavior in these three binary systems. It is also assumed that the Gibbs energy $g_{CaSi/OS}$ of the quadruplet in the center of Figure 1 is given by the weighted average of $g_{CaSi/OO}$, $g_{CaSi/SS}$, $g_{CaCa/OS}$, and $g_{SiSi/OS}$ as described in Reference 7. These assumptions are not requirements of the model; nonzero values of the parameters $\Delta g_{CaSi/SS}$, $\Delta g_{CaCa/OS}$, $\Delta g_{SiSi/OS}$, and $\Delta g_{CaSi/OS}$ could be included if necessary to reproduce experimental sulfide solubility data. However, the calculated sulfide solubilities are insensitive to the values of $\Delta g_{SiSi/OS}$ and $\Delta g_{CaSi/SS}$, and the CaO-CaS liquid system is, in fact, relatively ideal. Similarly, for all other systems i-j-O-S (i, j = Al^{3+}, Ca^{2+}, Fe^{2+}, Fe^{3+}, Mg^{2+}, Mn^{2+}, Si^{4+}, Ti^{3+}, Ti^{4+}), we have found that the assumption that these parameters are all zero yields calculated sulfide solubilities, which agree with measurements within experimental error limits in all cases.

Hence, the sulfide solubilities are predicted solely from the Gibbs energies of the pure liquid oxides and sulfides and from the SNN pair exchange Gibbs energies $\Delta g_{ij/OO}$, which are taken from our previous evaluations of oxide slags. This means that the change in the Gibbs energy of an oxide slag resulting from the addition of sulfide is mainly based on changes in FNN interaction energies and configurational entropy effects.

The model has been extended to multicomponent systems containing O^{2-} and S^{2-} with any number of cations.[7] In many cases, SNN pair exchange reactions have been evaluated/optimized as functions of composition in ternary, as well as in binary, oxide slags and are included in the current oxide slag database.

The equilibrium quadruplet concentrations $n_{ij/kl}$ for a given slag composition are calculated as those that minimize the total Gibbs energy G of the system. Hence, for any given slag composition, the chemical potentials of all components can be calculated. By using the database in conjunction with other evaluated databases for gases and for solid and liquid compounds and solutions, the sulfur solubilities can be calculated for a variety of equilibrium conditions, such as equilibrium with a gas phase of fixed oxygen and sulfur partial pressures, saturation with solid phases, or equilibrium with a liquid metallic solution.

III. GIBBS ENERGIES OF PURE LIQUID OXIDES AND SULFIDES

The Gibbs energies of the pure liquid oxides (SiO_2, CaO, *etc.*) in the current study are taken from our current oxide slag database. The Gibbs energies of the pure liquid sulfides are taken from standard compilations or estimated as follows:

Al_2S_3: $g°$ obtained by combining $g°$ of solid from JANAF[31] with temperature and enthalpy of fusion and liquid heat capacity from Barin *et al.*[32]
CaS: $g°$ obtained by combining $g°$ of solid from JANAF[31] with temperature of fusion from Holleman and Wiberg[33] and assuming that the entropy of fusion and liquid heat capacity are the same as for MnS.
FeS: g° from Waldner and Pelton.[34]
Fe_2S_3: As sulfide capacity data are available only for FeO-containing slags under reducing conditions, the calculations are insensitive to the assumed Gibbs energy of Fe_2S_3.
MgS: $g°$ obtained by combining $g°$ of solid from JANAF[31] with an entropy of fusion and liquid heat capacity assumed the same as those of MnS and with an enthalpy of fusion estimated as $\Delta H_{fus}(CaS) \times (\Delta H_{fus}(MgO)/\Delta H_{fus}(CaO))$.
MnS: $g°$ obtained by combining $g°$ of solid from Mills[35] with the temperature of fusion from Staffansson[36] and with the enthalpy of fusion from Coughlin.[37]
SiS_2: $g°$ from SGTE pure substance database.[38]
TiS_2: $g°$ obtained by combining $g°$ of solid from Barin *et al.*[32] with an enthalpy and temperature of fusion equal to those of ZrS_2, which were taken from the SGTE pure substance database[38], and assuming a heat capacity equal to that of solid TiS_2.[32]
Ti_2S_3: $g°$ obtained by combining $g°$ of solid from Mills[35] with an entropy of fusion assumed the same as that of Al_2O_3, with a liquid heat capacity assumed the same as that of solid Ti_2S_3[35], and with an enthalpy of fusion estimated as $\Delta H_{fus}(Al_2S_3) \times (\Delta H_{fus}(Ti_2O_3)/\Delta H_{fus}(Al_2O_3))$.

IV. SULFIDE CAPACITY

Sulfide solubilities in oxide slags are usually reported as "sulfide capacities," C_S, defined as[39]

$$C_S = (\text{wt pct S})\left(\frac{P_{O_2}}{P_{S_2}}\right)^{1/2} \qquad [8]$$

where (wt pct S) is the equilibrium sulfur content and P_{O_2} and P_{S_2} are the equilibrium partial pressures of O_2

and S_2, respectively. From the equilibrium constant of the general dissolution equation:

$$\left(O^{2-}\right) + \frac{1}{2}S_2(g) = \left(S^{2-}\right) + \frac{1}{2}O_2(g) \qquad [9]$$

it follows that, for a slag of a given oxide composition, C_S will be independent of (wt pct S), and P_{O_2} and P_{S_2} when the sulfur content is small (Henry's Law behavior). At higher sulfur contents, however, C_S will in general depend on P_{O_2} and P_{S_2}. In the next section, the calculated values of C_S are compared with experimental data. In all cases, the calculations were performed at the same values of P_{O_2} and P_{S_2} as were actually used in the experiments. Where P_{O_2} and P_{S_2} were not given, a small sulfur content in the slag was assumed.

In Figure 2 is a plot of the calculated equilibrium quadruplet concentrations in a liquid slag MO-SiO_2, containing a small amount of dissolved sulfur, at equilibrium with a gas phase in which $P_{O_2} = P_{S_2} = 10^{-10}$ bar, when the Gibbs energy of the exchange reaction (Eq. [1]) among the pure liquid components is given by:

$$\Delta g^{\text{exchange}}_{\text{MSi/OS}} = -350 \text{ kJ/mol} \qquad [10]$$

and the Gibbs energy of the SNN pair exchange reaction (Eq.[2]) is given by:

$$\Delta g_{\text{MSi/OO}} = -100 \text{ kJ/mol} \qquad [11]$$

As discussed above, these values are typical of systems in which MO is a basic oxide (CaO, MgO, MnO, *etc.*)

The negative value of $\Delta g_{\text{MSi/OO}}$ favors the formation of MSi/OO quadruplets. Hence, MO-SiO_2 solutions in which $X_{MO} > 2/3$ (where X_{MO} = mole fraction of MO) contain mainly MSi/OO and MM/OO quadruplets and few SiSi/OO quadruplets (that is, mainly free O^{2-} ions and singly bonded O^- and few O° oxygen "bridges"), whereas solutions in which $X_{MO} < 2/3$ consist mainly of MSi/OO and SiSi/OO quadruplets, with very few MM/OO quadruplets as can be seen in Figure 2. At the same time, the negative value of $\Delta g^{\text{exchange}}_{\text{MM/OS}}$ favors Si-O and M-S FNN pairs over Si-S and M-O pairs. Hence, in systems rich in MO, the principal S-containing quadruplets are MM/OS quadruplets, which contain no energetically unfavorable Si-S FNN pairs as observed in Figure 2. In solutions with $X_{MO} < 2/3$, however, where SNN M-O-M pairs are energetically unfavorable, the major S-containing quadruplets are MSi/OS quadruplets, because these contain no SNN M-O-M pairs and they contain fewer unfavorable Si-S FNN pairs than do SiSi/OS quadruplets. This can be viewed in Figure 2. Finally, the sum of the concentrations of all S-containing quadruplets is also shown in Figure 2. It will be observed in the next section that this curve is similar in shape to experimental curves of log C_S *vs* composition in MO-SiO_2 slags.

Finally, in basic systems at high sulfur contents, MM/SS quadruplets will become predominant.

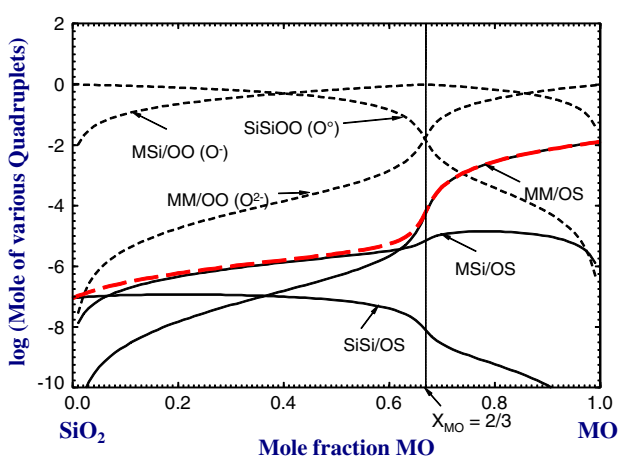

Fig. 2—Equilibrium concentrations of quadruplets in MO-SiO_2 melts at 1500 °C when $\Delta g_{\text{MSi/OO}} = -100$ kJ, $\Delta g^{\text{exchange}}_{\text{MSi/OS}} = -350$ kJ, and $P_{O_2} = P_{S_2} = 10^{-10}$ bar. The thick dashed line is the sum of sulfur-containing quadruplets.

V. COMPARISON OF CALCULATED AND EXPERIMENTAL SULFIDE CAPACITIES

A comparison of calculated (that is, predicted) sulfide capacities with all available experimental data for Al_2O_3-CaO-FeO-Fe_2O_3-MgO-MnO-SiO_2-TiO_2-Ti_2O_3 slags is presented in Figures 3 to 35. A summary of the sources of experimental data are given in Table I along with the experimental conditions of temperature, P_{O_2} and P_{S_2} in each case.

From Figures 3 to 35, it can be clearly observed that the data are often scattered and that disagreement among different studies is often considerable. In essentially all cases, the calculations agree with the reported data within the error limits of the latter. We shall not comment here on every figure but only when such comment is required for clarification.

It should be noted that sulfide capacities are sometimes reported in slags below their liquidus temperature. In such cases, it is usually not clear whether the measurements were made in a two-phase solid/liquid region or in a metastable undercooled single-phase liquid. The model calculations are always reported for

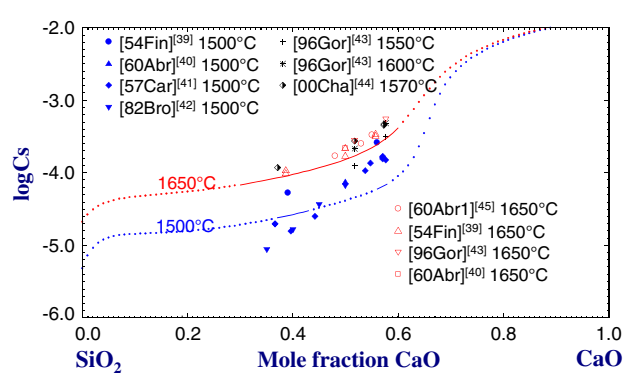

Fig. 3—Calculated sulfide capacity in CaO-SiO_2 melts at $P_{O_2} = 10^{-9}$, $P_{S_2} = 10^{-2}$ $P_{O2} = 10^{-9}$, $P_{S2} = 10^{-2}$ bar compared with experimental data.[39–45] The dashed lines are subliquidus.

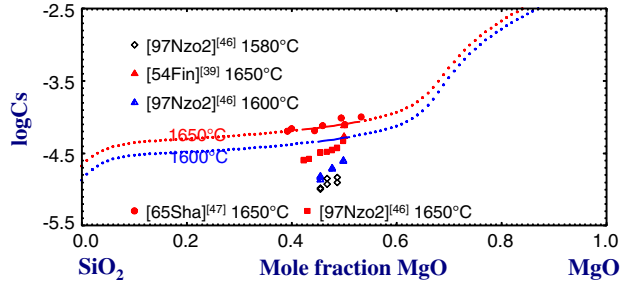

Fig. 4—Calculated sulfide capacity in MgO-SiO_2 melts at $P_{O_2} = 10^{-8}$, $P_{S_2} = 10^{-4}$ bar compared with experimental data.[39,46,47] The dashed lines are subliquidus.

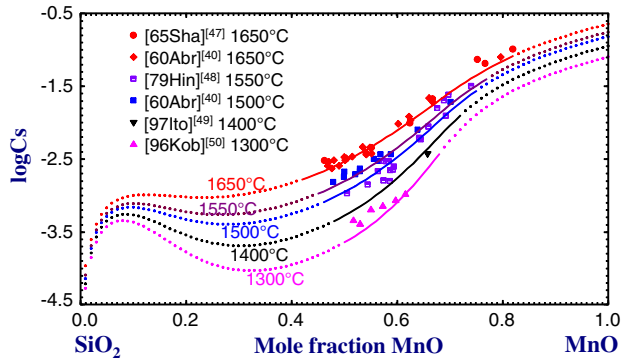

Fig. 5—Calculated sulfide capacity in MnO-SiO_2 melts at $P_{O_2} = 10^{-8}$, $P_{S_2} = 10^{-6}$ bar compared with experimental data.[40,47–50] The dashed lines are subliquidus.

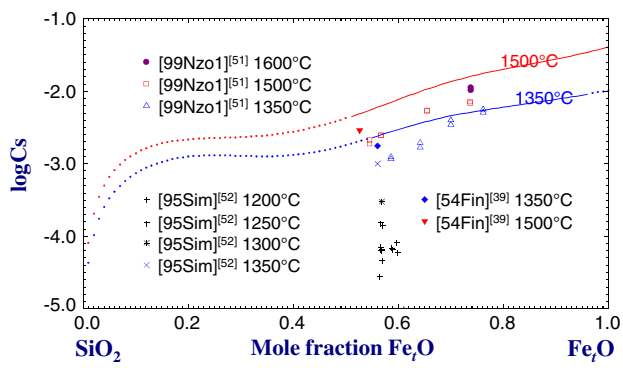

Fig. 6—Calculated sulfide capacity in Fe_tO-SiO_2 melts at $P_{O_2} = 10^{-7}$, $P_{S_2} = 10^{-3}$ bar compared with experimental data.[39,51,52] The dashed lines are subliquidus.

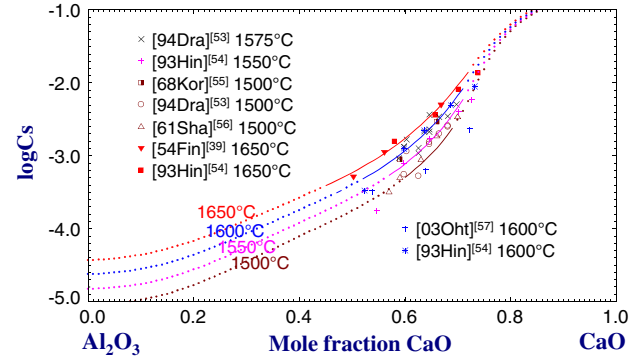

Fig. 7—Calculated sulfide capacity in CaO-Al_2O_3 melts at $P_{O_2} = 10^{-7}$, $P_{S_2} = 10^{-3}$ bar compared with experimental data.[39,53–57] The dashed lines are subliquidus.

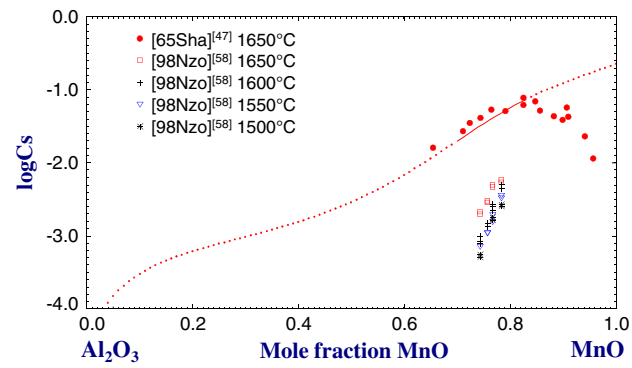

Fig. 8—Calculated sulfide capacity in MnO-Al_2O_3 melts at $P_{O_2} = 10^{-8}$, $P_{S_2} = 10^{-6}$ bar compared with experimental data.[47,58] The dashed lines are subliquidus.

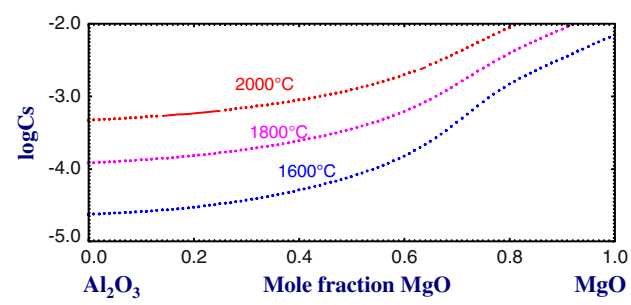

Fig. 9—Calculated sulfide capacity in MgO-Al_2O_3 melts at $P_{O_{10}} = 10^{-9}$, $P_{S_2} = 10^{-5}$ bar. The dashed lines are subliquidus.

single-phase liquid slags, either stable or metastable. In Figures 3 to 35, the calculated lines are shown as dashed lines when the temperature is below the liquidus (as calculated by FactSage[9]).

According to Abraham *et al.*,[40] in Figure 6 for the Fe_tO-SiO_2 system, the original data reported by Fincham and Richardson[39] were incorrect because of errors in the calculation of the gas partial pressures. The points shown in Figure 6 are the corrected values.

For the MnO-Al_2O_3 system, some data[47] were reported below the liquidus as observed in Figure 8. The disagreement with the calculated curve suggests that the measurements were made in two-phase solid/liquid mixtures. No data are available for the MgO-Al_2O_3 system. The calculated curves are shown in Figure 9. In all systems in which "Fe_tO" is shown as a component, the calculations take into account both Fe^{2+} and Fe^{3+} in the melts; the equilibrium Fe^{2+}/Fe^{3+} ratio was calculated for the oxygen partial pressure given in the figure caption. Similarly, in all systems in which "TiO_x" appears as a component, both Ti^{3+} and Ti^{4+} are taken into account in the calculations.

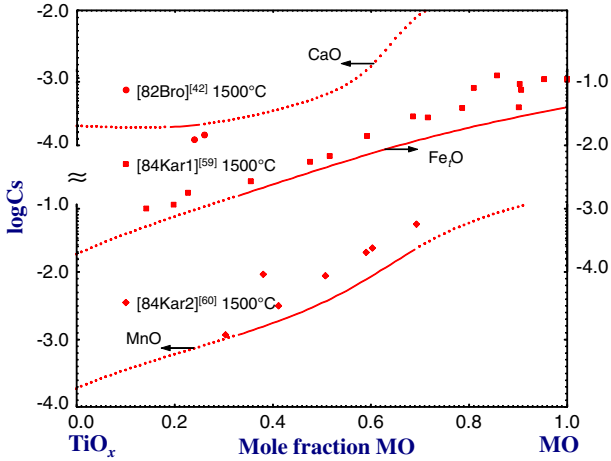

Fig. 10—Calculated sulfide capacities in CaO-TiO$_x$, Fe$_t$O-TiO$_x$, and MnO-TiO$_x$ melts compared with experimental data.[42,59,60] Calculations at $P_{O_2} = 10^{-9}$, $P_{S_2} = 10^{-3}$ bar for CaO-TiO$_x$; $P_{O_2} = 10^{-7}$, $P_{S_2} = 10^{-4}$ bar for Fe$_t$O-TiO$_x$ and MnO-TiO$_x$ slags. The dashed lines are subliquidus.

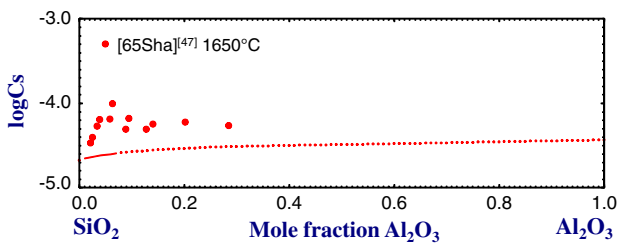

Fig. 11—Calculated sulfide capacity in Al$_2$O$_3$-SiO$_2$ melts at $P_{O_2} = 10^{-10}$, $P_{S_2} = 10^{-5}$ bar compared with experimental data.[47] The dashed lines are subliquidus.

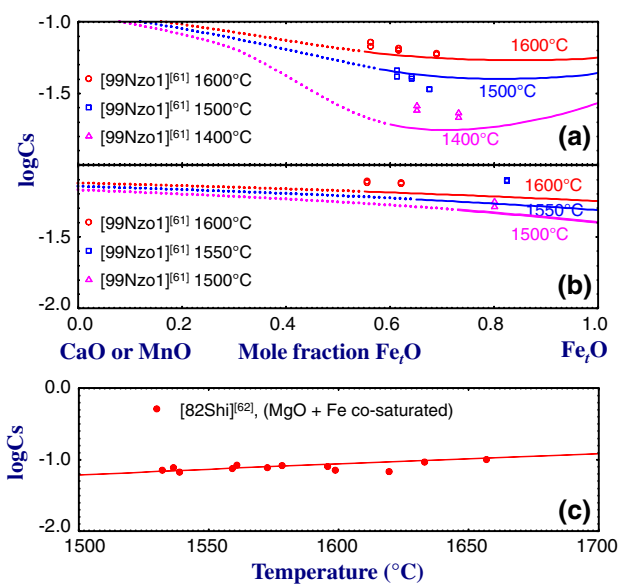

Fig. 12—Calculated sulfide capacities compared with experimental data[61,62] in (*a*) CaO-Fe$_t$O melts at 1600 °C when $P_{O_2} = 10^{-7}$, $P_{S_2} = 10^{-2}$, and at 1400 °C and 1500 °C when $P_{O_2} = 10^{-8}$, $P_{S_2} = 10^{-3}$ bar; (*b*) MnO-Fe$_t$O melts at $P_{O_2} = 10^{-7}$, $P_{S_2} = 10^{-2}$ bar; (*c*) Fe$_t$O-MgO melts cosaturated with MgO and Fe. The dashed lines are subliquidus.

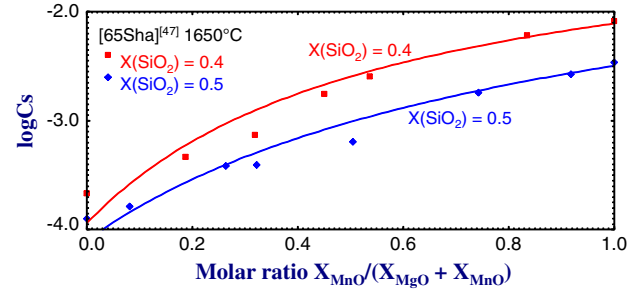

Fig. 13—Calculated sulfide capacity in MgO-MnO-SiO$_2$ melts at constant SiO$_2$ mole fraction at $P_{O_2} = 10^{-8}$, $P_{S_2} = 10^{-3}$ bar compared with experimental data.[47]

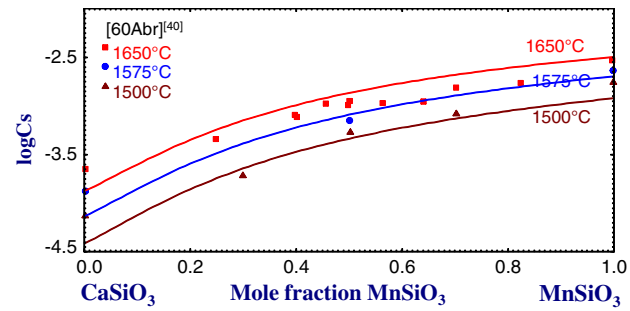

Fig. 14—Calculated sulfide capacity in CaO-MnO-SiO$_2$ melts along the CaSiO$_3$-MnSiO$_3$ join at $P_{O_2} = 10^{-7}$, $P_{S_2} = 10^{-3}$ bar compared with experimental data.[40]

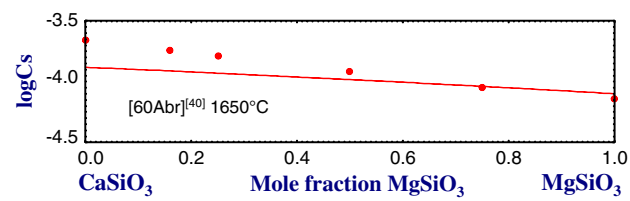

Fig. 15—Calculated sulfide capacity in CaO-MgO-SiO$_2$ melts along the CaSiO$_3$-MgSiO$_3$ join at $P_{O_2} = 10^{-7}$, $P_{S_2} = 10^{-3}$ bar compared with experimental data.[40]

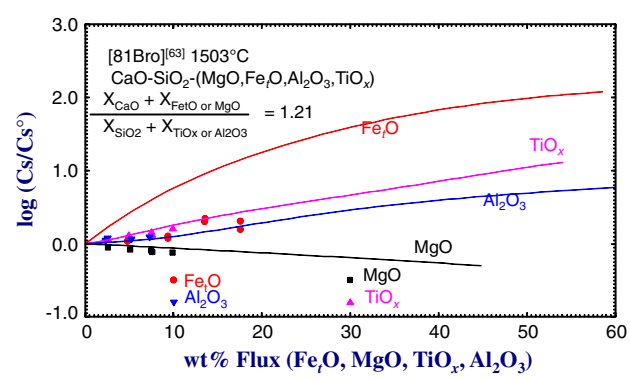

Fig. 16—Calculated sulfide capacity ratio ($C_S/C_S°$) at 1503 °C showing effect of additives to a CaO-SiO$_2$ melt with initial molar ratio X_{CaO}/X_{SiO_2} = 1.21 compared with experimental data,[63] where $C_S°$ is the sulfide capacity of initial CaO-SiO$_2$ slag as reported by Abraham and Richardson.[45] Calculations at $P_{O_2} = 10^{-8}$, $P_{S_2} = 10^{-3}$ bar.

Although closer agreement with the reported data in the SiO_2-Al_2O_3 system in Figure 11 could be obtained by slightly adjusting certain model parameters, any such adjustments yield poorer agreement in the acidic regions of systems with three or more oxides containing SiO_2 or Al_2O_3. The agreement in Figure 11 is within experimental error limits in any case.

In some experimental studies of systems with three or more oxide components, measurements were made at points along simple composition paths. In these cases, comparisons of calculated and experimental sulfide capacities are shown along these paths as in Figures 13

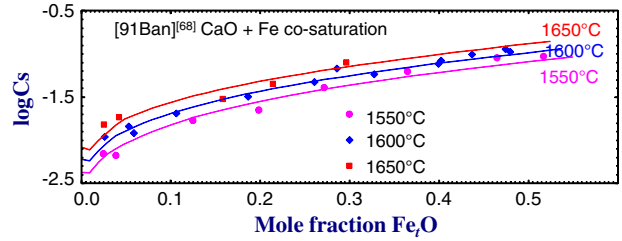

Fig. 19—Calculated sulfide capacity in CaO-Fe$_t$O-Al_2O_3 melts cosaturated with CaO and Fe compared with experimental data.[68]

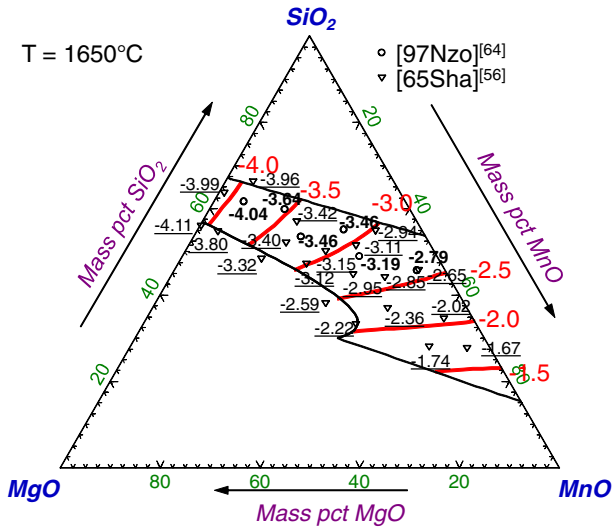

Fig. 17—Calculated iso-log(C_S) lines in MgO-MnO-SiO_2 melts at $P_{O_2} = 10^{-7}$, $P_{S_2} = 10^{-2}$ bar compared with experimental data.[56,64]

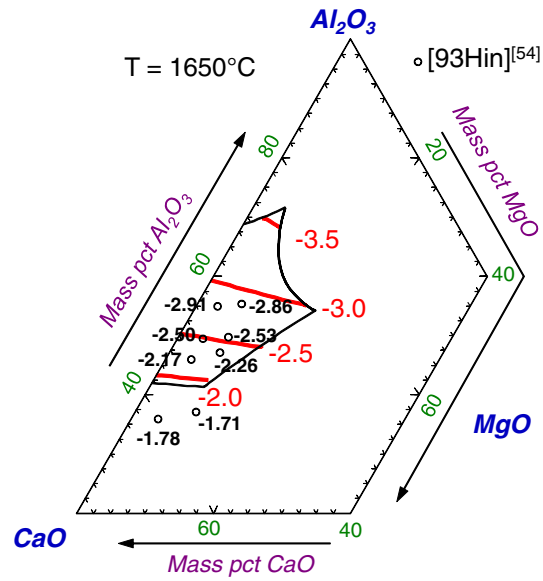

Fig. 20—Calculated iso-log(C_S) lines in CaO-MgO-SiO_2 melts at $P_{O_2} = 10^{-7}$, $P_{S_2} = 10^{-3}$ bar compared with experimental data.[54]

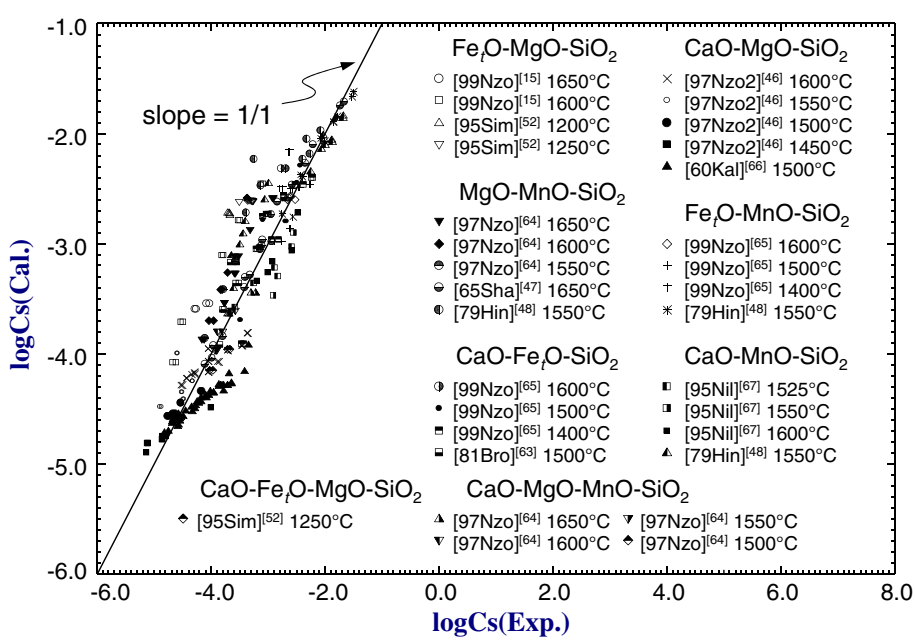

Fig. 18—Comparison of experimental[15,46–48,52,63–67] and calculated sulfide capacities for MO-NO-····-SiO_2 type melts. Calculations were carried out for oxygen and sulfur partial pressures corresponding to the experimental conditions.

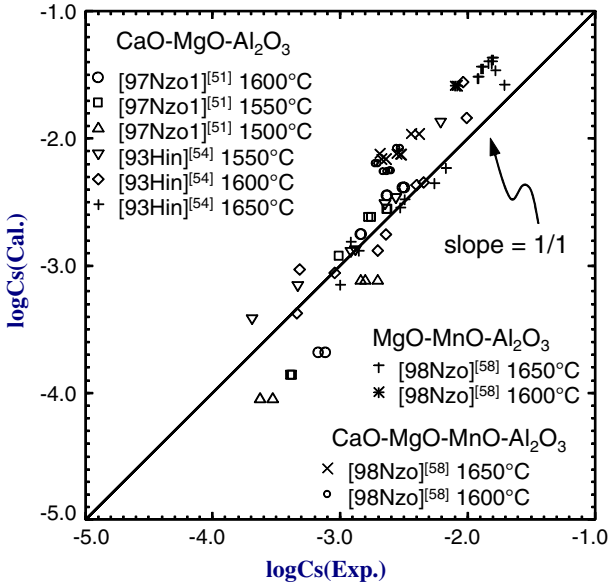

Fig. 21—Comparison of experimental[51,54,58] and calculated sulfide capacities for MO-NO-···-Al_2O_3 type melts. Calculations were carried out for oxygen and sulfur partial pressures corresponding to the experimental conditions.

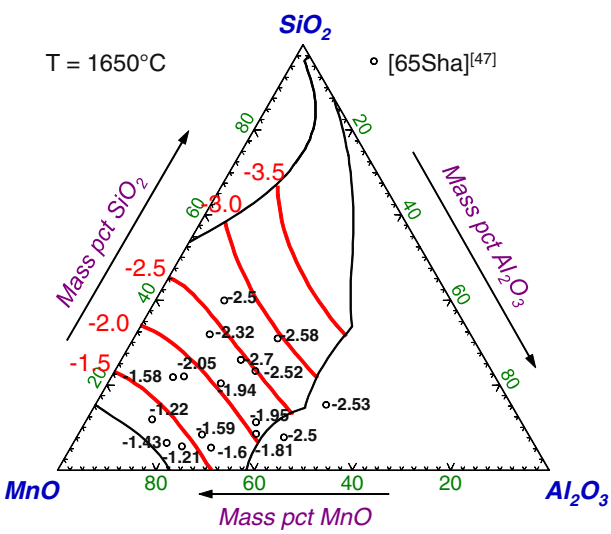

Fig. 22—Calculated iso-log(C_S) lines in MnO-SiO_2-Al_2O_3 melts at $P_{O_2} = 10^{-7}$, $P_{S_2} = 10^{-3}$ bar compared with experimental data.[47]

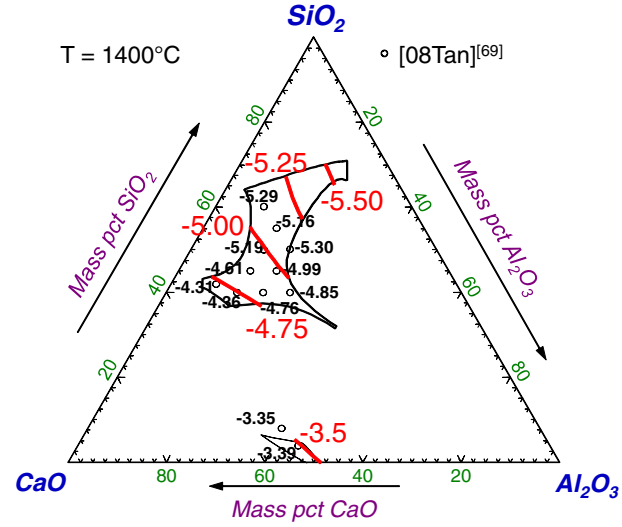

Fig. 23—Calculated iso-log(C_S) lines in CaO-SiO_2-Al_2O_3 melts at $P_{O_2} = 10^{-7}$, $P_{S_2} = 10^{-3}$ bar compared with experimental data.[69]

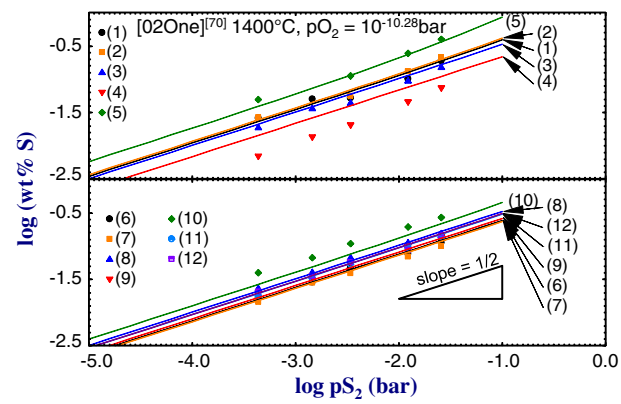

Fig. 24—Calculated sulfur content of CaO-MgO-Al_2O_3-SiO_2 melts at $P_{O2} = 10^{-10.28}$ bar at 1400 °C as a function of P_{S2} compared with experimental data[70] for melt compositions (wt pct): (1) 24.5CaO-10.2MgO-15Al_2O_3-50.3SiO_2, (2) 21.2-16.4-12.7-49.7, (3) 15.1-20.8-9.1-54.9, (4) 16.4-6.6-9.9-66.8, (5) 39.6-4-6.1-50.9, (6) 16.0-11.8-15.1-56.7, (7) 8.6-19.6-13.7-57.7, (8) 16.1-19.2-6.3-58.3, (9) 12.4-17.9-21.1-48.3, (10) 21.1-18.7-9.9-50.1, (11) 18.1-13.2-5.7-62.8, and (12) 25.4-2.2-11.8-60.1.

to 16, 19, 26 to 28, and 30 to 32. In other studies, measurements were not made along simple composition paths. In these cases, the results are plotted as iso-C_S lines on a composition triangle and compared with all data points as in Figures 17, 20, 22, and 23, or else calculated and experimental log C_S values are plotted as axes as in Figures 18, 21, 29, and 35.

In Figure 13, the experimental data can be seen to exhibit a deviation from linearity as the molar ratio $X_{MnO}/(X_{MgO} + X_{MnO})$ varies from 0.0 to 1.0 at constant SiO_2 mole fraction. The calculations reproduce this deviation from linearity. In the model, this results from the fact that SNN SRO is stronger in the MgO-SiO_2 system than in the MnO-SiO_2 system because $\Delta g_{MgSi/OO} < \Delta g_{MnSi/OO}$. That is, MgSi/OO quadruplets are thermodynamically more stable than MnSi/OO quadruplets. Hence, as Mn is progressively replaced by Mg at constant SiO_2 content, Mg and Si tend to form clusters of MgSi/OO quadruplets whereas Mn forms regions of MnMn/OO clusters that contain relatively little Si. Because Si-S pairs are unfavorable energetically, sulfur is relatively more soluble in the regions of MnMn/OO clusters. Similar behavior is observed in Figure 14 for the CaO-MnO-SiO_2 system, whereas in Figure 15 for the CaO-MgO-SiO_2 system, virtually no deviation from linearity is observed because $\Delta g_{CaSi/OO} \approx \Delta g_{MgSi/OO}$. It is noteworthy that the current model predicts this nonlinearity. The earlier RBP model predicts linear behavior.

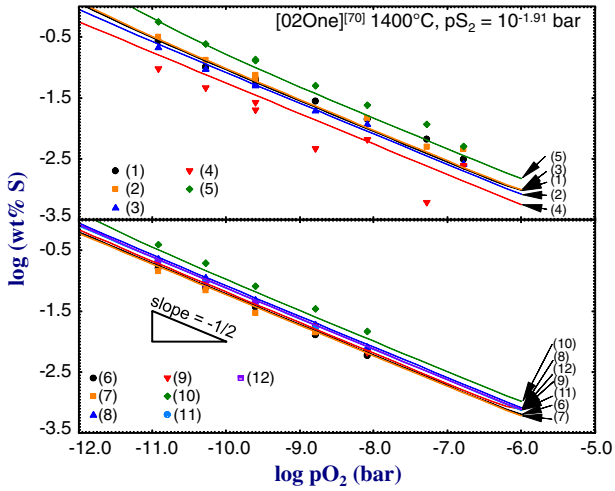

Fig. 25—Calculated sulfur content of CaO-MgO-Al_2O_3-SiO_2 melts at $P_{S_2} = 10^{-1.91}$ bar as function of P_{O_2} compared with experimental data.[70] Melt compositions are the same as in Figure 24.

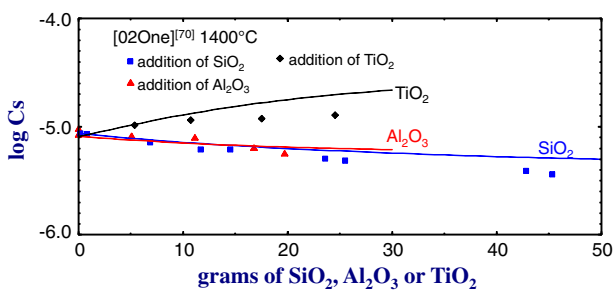

Fig. 26—Calculated sulfide capacities showing effect of additives to 100 g of a melt of composition (wt pct) 24.5CaO-10.2MgO-15.0Al_2O_3-50.3SiO_2. Calculations at $P_{O_2} = 10^{-10.92}$, $P_{S_2} = 10^{-1.91}$ bar for SiO_2 additions; $P_{O_2} = 10^{-9.6}$, $P_{S_2} = 10^{-1.91}$ bar for Al_2O_3 and TiO_2 additions.

In Figure 16, calculated and experimental[63] sulfide capacities are compared for various additions to CaO-SiO_2 melts with an initial molar ratio X_{CaO}/X_{SiO_2}. Agreement between the calculations and the experimental results is good except for the case of Fe_tO additions. However, the oxygen partial pressure during the experiments was not reported. The calculations were performed under the assumption of a low oxygen partial pressure so that Fe is present mainly as Fe^{2+}. If the calculations are performed at higher P_{O_2}, with a resultant increase in Fe^{3+} content, then the experimental data are reproduced.

In Figure 35, the results of Brown *et al.*[42] for CaO-SiO_2-TiO_x slag were performed at low oxygen partial pressures ($P_{O_2} \approx 10^{-14}$ bar) where Ti^{3+} is predominant over Ti^{4+}. The calculations were made for the same oxygen partial pressure.

VI. COMPARISON OF CALCULATED AND EXPERIMENTAL PHASE DIAGRAMS

The current model is not limited to melts dilute in sulfur but applies at all compositions from pure liquid oxide to pure liquid sulfide. In the following comparisons of the calculations with experimental phase diagrams, no new adjustable model parameters were introduced; the calculations are predictions based solely on the optimized model parameters for the sulfur-free oxide systems and the Gibbs energies of the pure liquid sulfides. For the solid oxide phases, optimized thermodynamic properties from the FactSage[9] databases were used. For solid MnS, data were taken from Mills.[35] All solid phases were assumed to be pure stoichiometric compounds (no solid solutions).

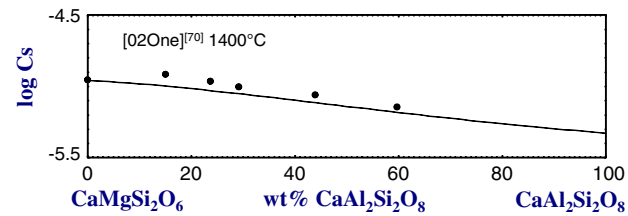

Fig. 27—Calculated sulfide capacity in CaO-MgO-Al_2O_3-SiO_2 melts along the diopside ($CaMgSi_2O_6$) – anorthite ($CaAl_2Si_2O_8$) join at $P_{O_2} = 10^{-9.6}$, $P_{S_2} = 10^{-1.91}$ bar compared with experimental data.[70]

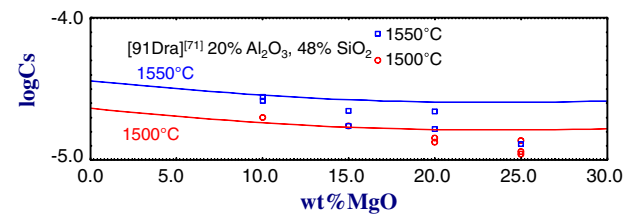

Fig. 28—Calculated sulfide capacity in Al_2O_3-CaO-MgO-SiO_2 melts at $P_{O_2} = 10^{-7}$, $P_{S_2} = 10^{-3}$ bar at constant content of Al_2O_3(20 wt pct) and SiO_2(48 wt pct).

A. *MnO-MnS System*

The calculated phase diagram is compared with the available data in Figure 36. As discussed, the liquid phase was assumed to be ideal. Given the wide scatter of the data, no additional model parameters are justified.

B. *MnO-MnS-SiO_2 System*

Calculated isothermal sections and the calculated $MnSiO_3$-MnS join are compared with experimental data in Figures 37 and 38. A ternary compound of the approximate formula $8MnO{\cdot}3SiO_2{\cdot}MnS$ has been observed.[78,81] This compound melts congruently between 1250 °C and 1350 °C and has only a small liquidus field. In the current calculations, the Gibbs energy of formation of $8MnO{\cdot}3SiO_2{\cdot}MnS$ from MnO, SiO_2(tridymite) and MnS was set to (76,241 – 140T) J/mol to reproduce the reported liquidus points in Figures 37(a) and (b). It can be observed that the agreement between the calculations and the reported data points[78,81,84] is essentially within experimental error limits in Figures 37 and 38, with the possible exception of the section at 1500 °C in Figure 37(f), even though no ternary model parameters were used.

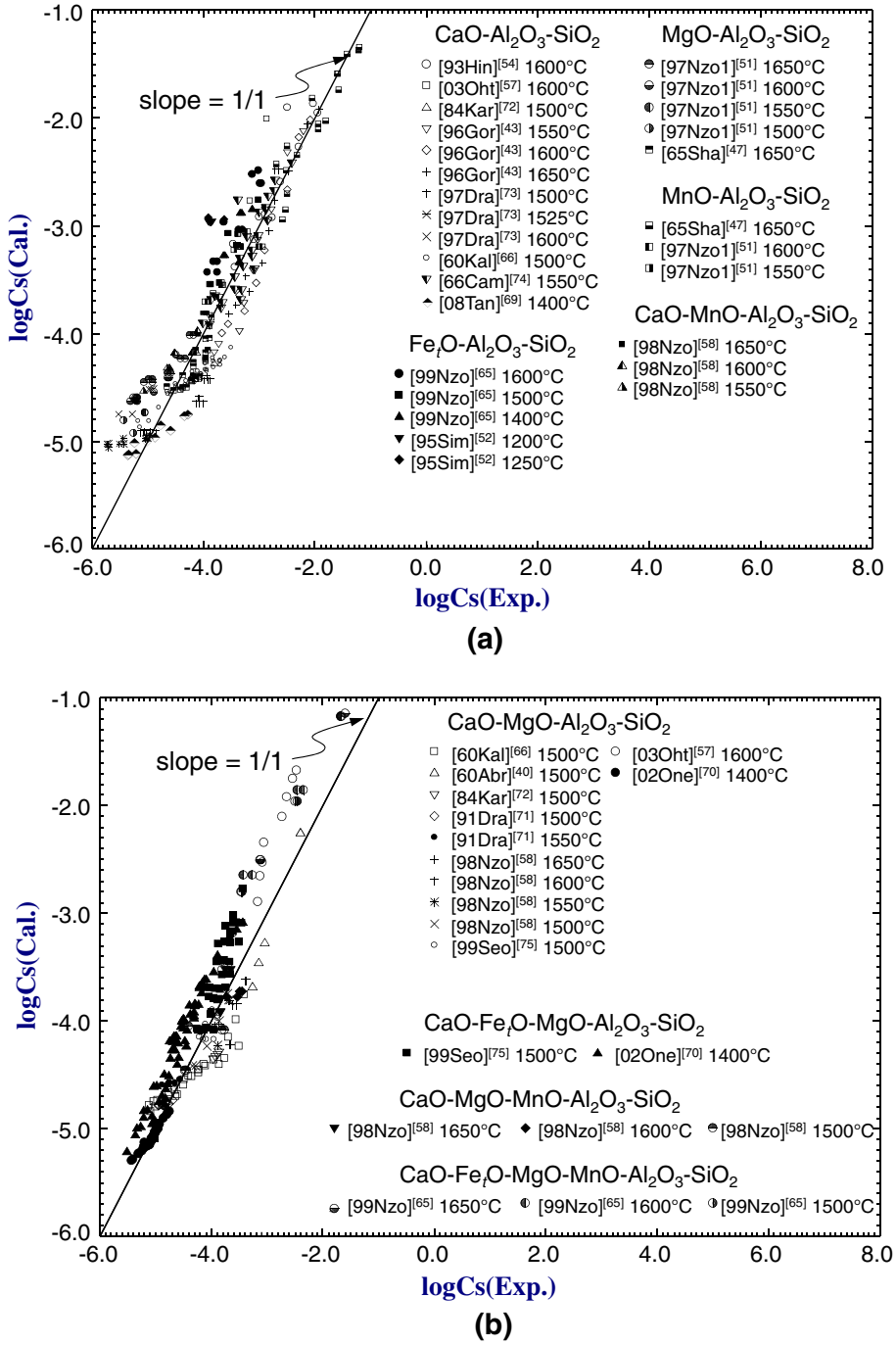

Fig. 29—Comparison of experimental[40,43,47,51,52,54,57,58,65,66,69,71–75] and calculated sulfide capacities for MO-NO-· · ·-Al_2O_3-SiO_2 type slags. Calculations were carried out for oxygen and sulfur partial pressures corresponding to the experimental conditions.

C. *MnO-MnS-Al_2O_3 System*

The calculated isothermal section at 1500 °C is compared with the data of Woo *et al.*[78] in Figure 39. The reported MnO liquidus is well reproduced by the calculations, although a discrepancy is found in the case of the $MnAl_2O_4$ liquidus. Also shown on Figure 39 is the reported[78] liquid composition for (MnO + $MnAl_2O_4$) cosaturation at 1400 °C. This point is reproduced within 2 wt pct by the calculations. Because the cosaturation point lies on the $MnAl_2O_4$ liquidus, the data of Woo *et al.*[78] show virtually no shift in the position of the liquidus between 1400 °C and 1500 °C. This seems unlikely and suggests that the data may be in error.

VII. DISCUSSION

A similar approach has been used to model solubilities in oxide slags of other gaseous species, such as

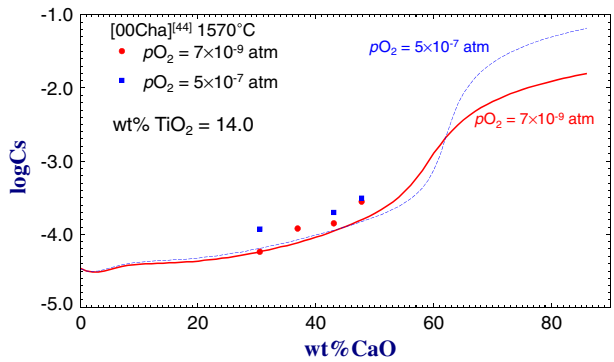

Fig. 30—Calculated sulfide capacity in $CaO\text{-}SiO_2\text{-}TiO_x$ melts containing 14 wt pct TiO_2 compared with experimental data.[44] Calculations at $P_{O_2} = 10^{-7}$, $P_{S_2} = 10^{-1}$, and $P_{O_2} = 7 \times 10^{-9}$, $P_{S_2} = 10^{-1.4}$ bar.

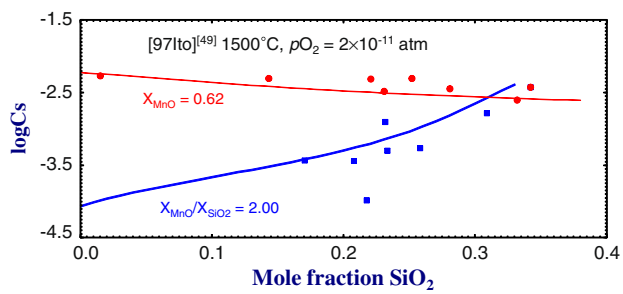

Fig. 31—Calculated sulfide capacity in $MnO\text{-}SiO_2\text{-}TiO_x$ melts at $P_{O_2} = 2 \times 10^{-11}$, $P_{S_2} = 10^{-5}$ bar compared with experimental data.[49]

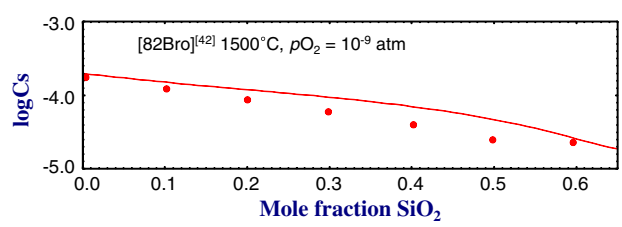

Fig. 32—Calculated sulfide capacity in $CaO\text{-}MgO\text{-}TiO_x\text{-}SiO_2$ melts at constant mole fractions $X_{CaO} = 0.2$ and $X_{MgO} = 0.15$ at $P_{O_2} = 10^{-19}$, $P_{S_2} = 10^{-3}$ bar compared with experimental data.[42]

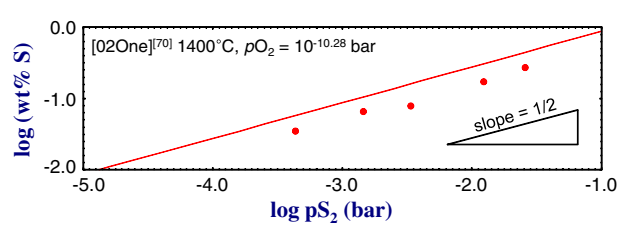

Fig. 33—Calculated sulfur content in a $19.6CaO\text{-}8.0MgO\text{-}11.8Al_2O_3\text{-}40.2SiO_2\text{-}19.9TiO_2$ (wt pct) melt at $P_{O_2} = 10^{-10.28}$ bar as a function of P_{S_2}.

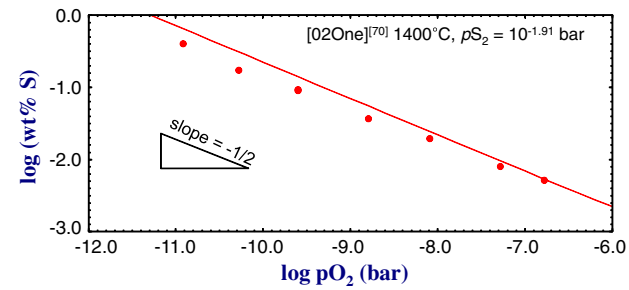

Fig. 34—Calculated sulfur content in a $19.6CaO\text{-}8.0MgO\text{-}11.8Al_2O_3\text{-}40.2SiO_2\text{-}19.9TiO_2$ (wt pct) melt at $P_{S_2} = 10^{-1.91}$ bar as a function of P_{O_2}.

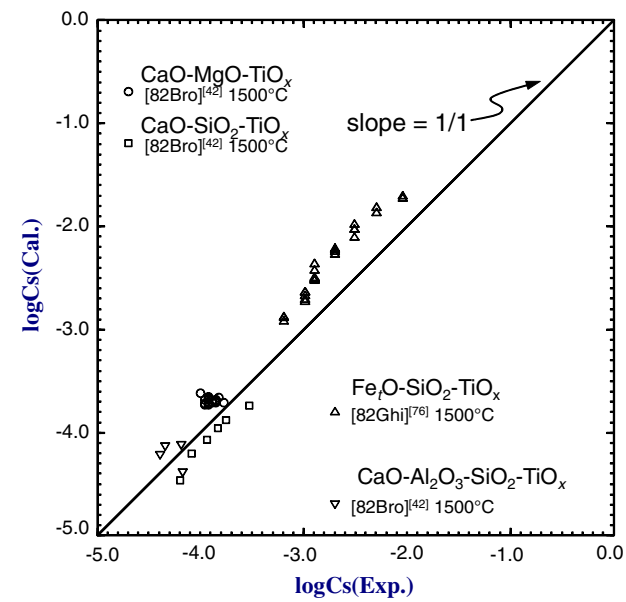

Fig. 35—Comparison of experimental[42,76] and predicted sulfide capacities for $MO\text{-}(NO\text{-}Al_2O_3\text{-}SiO_2)\text{-}TiO_x$ type melts. Calculations were carried out for oxygen and sulfur partial pressures corresponding to the experimental conditions.

sulfate, nitride, carbide, and water. For example, water dissolution in slags has been modeled as (Ca^{2+}, Al^{3+}, Si^{4+}, Mg^{2+}, ..., H^+)(O^{2-}, OH^-). Good agreement with experimental solubility data has been obtained as will be shown in subsequent articles.

The fact that no model parameters for SNN interactions involving sulfide ions were required to reproduce the available data shows that the change in the Gibbs energy of an oxide slag resulting from the addition of sulfide is mainly caused by changes in FNN interaction energies and configurational entropy effects.

Calculations of sulfide capacities of slags that contain Na_2O were also performed. With no additional adjustable model parameters, the calculations were not in close agreement with the available data, although good agreement could be obtained by including additional SNN pair exchange energy parameters. Because no such

Table I. References for Sulfide Capacity Measurements Showing Experimental Conditions

Reference	T (°C)	P_{O_2}(bar)	P_{S_2}(bar)
$CaO-SiO_2$			
[54Fin][39]**	1500	—	—
	1650	10^{-8}, 10^{-6}	1.2×10^{-3}, 7.8×10^{-5}
[60Abr][40]	1500	—	—
	1650	—	—
[57Car][41]**	1500	3.0×10^{-9}	1.7×10^{-3}
		$\sim 1.0 \times 10^{-8}$	$\sim 1.2 \times 10^{-2}$
[82Bro][42]	1500	—	—
[96Gor][43]	1550	—	—
	1600	—	—
	1650	—	—
[00Cha][44]	1570	7.0×10^{-9}, 5.0×10^{-7}	—
[60Abr1][45]	1650	—	—
$MgO-SiO_2$			
[54Fin][39]**	1650	10^{-8}, 10^{-6}	1.2×10^{-3}, 7.8×10^{-5}
[65Sha][47]	1650	—	—
[97Nzo2][46]	1580	—	—
	1600	2.0×10^{-7}	6.9×10^{-3}
	1650	4.6×10^{-7}	5.3×10^{-3}
$MnO-SiO_2$			
[60Abr][40]	1500	—	—
	1650		
[65Sha][47]	1650	—	—
[79Hin][48]	1550	10^{-7}	10^{-5} to 10^{-3}
[96Kob][50]†	1300	$10^{-12.4}$	—
[97Ito][49]‡	1400	2.0×10^{-11}	—
Fe_tO-SiO_2			
[99Nzo1][61]	1350	1.0×10^{-8}	4.0×10^{-3}
	1500	8.2×10^{-8}	4.4×10^{-3}
	1600	2.0×10^{-7}	7.1×10^{-3}
[54Fin][39]**	1350	1.1×10^{-8}	1.5×10^{-5}
	1500	1.7×10^{-7}	5.9×10^{-7}
[95Sim][52]	1200	$10^{-11 \text{ to } -9.5}$	$10^{-4.5 \text{ to } -3}$
	1250	$10^{-10.5 \text{ to } -10}$	10^{-3}
	1300	10^{-10}	10^{-3}
	1350	$10^{-10.5}$	10^{-3}
$CaO-Al_2O_3$			
[68Kor][55]	1500	—	—
[61Sha][56]	1500	—	—
[54Fin][39]**	1650	10^{-8}, 10^{-6}	1.2×10^{-3}, 7.8×10^{-5}
[93Hin][54]	1550	7.0×10^{-8}	8.4×10^{-4}
	1600	1.8×10^{-7}	5.2×10^{-4}
	1650	4.5×10^{-7}	3.1×10^{-4}
[03Oht][57]‡	1600	6.9×10^{-11}	—
[94Dra][53]	1500	5.7×10^{-8}	7.3×10^{-3}
	1575	2.1×10^{-7}	4.7×10^{-3}
$MnO-Al_2O_3$			
[98Nzo][58]	1500	8.6×10^{-8}	4.2×10^{-3}
	1550	2.2×10^{-7}	2.8×10^{-3}
	1600	2.0×10^{-7}	6.9×10^{-3}
	1650	4.6×10^{-7}	5.3×10^{-3}
[65Sha][47]	1650	—	—
$CaO-TiO_x$			
[82Bro][42]	1500	10^{-9}	10^{-3}
$MgO-MnO-SiO_2$			
[97Nzo][64]	1550	2.2×10^{-7}	2.8×10^{-3}
	1600	2.0×10^{-7}	6.9×10^{-3}
	1650	4.6×10^{-7}	5.3×10^{-3}
[65Sha][47]	1650	—	—
[79Hin][48]	1550	10^{-7}	10^{-5} to 10^{-3}
$CaO-Fe_tO-MgO-SiO_2$			
[95Sim][52]	1250	10^{-10}	10^{-3}
$CaO-MgO-MnO-SiO_2$			
[97Nzo][64]	1500	8.6×10^{-8}	4.2×10^{-3}
	1550	2.2×10^{-7}	2.8×10^{-3}
	1600	2.0×10^{-7}	6.9×10^{-3}
	1650	4.6×10^{-7}	5.3×10^{-3}
$CaO-Fe_tO-Al_2O_3$			
[91Ban][68]§	1550 ~1650	—	—
$CaO-MgO-Al_2O_3$			
[93Hin][54]	1550	7.0×10^{-8}	8.4×10^{-4}
	1600	1.8×10^{-7}	5.2×10^{-4}
	1650	4.5×10^{-7}	3.1×10^{-4}
[97Nzo1][51]	1500	8.6×10^{-8}	4.2×10^{-3}
	1550	2.2×10^{-7}	2.8×10^{-3}
	1600	2.0×10^{-7}	6.9×10^{-3}
$MgO-MnO-Al_2O_3$			
[98Nzo][58]	1600	2.0×10^{-7}	6.9×10^{-3}
	1650	4.6×10^{-7}	5.3×10^{-3}
$Al_2O_3-SiO_2$			
[65Sha][47]	1650	—	—
$CaO-Al_2O_3-SiO_2$			
[93Hin][54]	1550	7.0×10^{-8}	8.4×10^{-4}
	1600	1.8×10^{-7}	5.2×10^{-4}
	1650	4.5×10^{-7}	3.1×10^{-4}
[81Bro][63]	1503	—	—
[60Kal][66]	1500	—	—
[60Abr1][45]	1650	—	—
[03Oht][57]‡	1600	6.9×10^{-11}	—
[97Dra][73]	1500	5.6×10^{-8}	7.3×10^{-3}
	1525	1.0×10^{-7}	4.7×10^{-3}
		$\sim 2.0 \times 10^{-7}$	$\sim 1.0 \times 10^{-2}$
		3.0×10^{-7}	4.0×10^{-3}
	1600	$\sim 1.5 \times 10^{-5}$	$\sim 9.0 \times 10^{-1}$
[84Kar][72]	1500	—	—
[96Gor][43]**	1550	3.1×10^{-8}	8.2×10^{-3}
	1600	7.7×10^{-8}	7.0×10^{-4}
	1650	1.8×10^{-7}	5.7×10^{-4}
[08Tan][69]	1400	—	—
$Fe_tO-Al_2O_3-SiO_2$			
[95Sim][52]	1200	10^{-11}, $10^{-11 \text{ to } -10}$	$10^{-4.5 \text{ to } -3}$, 10^{-3}
[99Nzo][65]	1400	3.6×10^{-8},	1.5×10^{-3},
	1500	8.2×10^{-8},	4.4×10^{-3},
	1600	2.0×10^{-7}	7.1×10^{-3}
$MgO-Al_2O_3-SiO_2$			
[97Nzo1][51]	1500	8.6×10^{-8}	4.2×10^{-3}
	1550	2.2×10^{-7}	2.8×10^{-3}
	1600	2.0×10^{-7}	6.9×10^{-3}
	1650	4.6×10^{-7}	5.3×10^{-3}
[65Sha][47]	1650	—	—

Table I. continued

Reference	T (°C)	P_{O_2}(bar)	P_{S_2}(bar)
Fe_tO-TiO_x			
[84Kar1][59]	1500	1.0×10^{-7}	3.7×10^{-4}
		$\sim 1.0 \times 10^{-6}$	$\sim 7.8 \times 10^{-6}$
MnO-TiO_x			
[84Kar2][60]	1500	1.0×10^{-7}	3.7×10^{-4}
		$\sim 1.0 \times 10^{-6}$	$\sim 7.8 \times 10^{-6}$
Fe_tO-CaO			
[99Nzo1][61]	1400	3.6×10^{-8}	1.5×10^{-3}
	1500	8.2×10^{-8}	4.4×10^{-3}
	1600	2.0×10^{-7}	7.1×10^{-3}
Fe_tO-MnO			
[99Nzo1][61]	1500	8.6×10^{-8}	4.2×10^{-3}
	1550	2.2×10^{-7}	2.8×10^{-3}
	1600	2.0×10^{-7}	6.9×10^{-3}
Fe_tO-MgO			
[82Shi][62]*	1525	—	—
	~1650		
CaO-Fe_tO-SiO_2			
[81Bro][63]	1503	—	—
[99Nzo][65]	1400	3.6×10^{-8}	1.5×10^{-3}
	1500	8.2×10^{-8}	4.4×10^{-3}
	1600	2.0×10^{-7}	7.1×10^{-3}
CaO-MgO-SiO_2			
[81Bro][63]	1503	—	—
[60Kal][66]	1500	—	—
[60Abr][40]	1500	—	—
	~1650		
[65Sha][56]	1650	—	—
[97Nzo2][46]	1450		
	1500	8.2×10^{-8}	4.4×10^{-3}
	1600	2.0×10^{-7}	6.9×10^{-3}
	1650	4.6×10^{-7}	5.3×10^{-3}
CaO-MnO-SiO_2			
[60Abr][40]	1500	—	—
	~1650		
[65Sha][56]	1650	—	—
[79Hin][48]	1550	10^{-7}	10^{-5} to 10^{-3}
[95Nil][67]	1525	1.1×10^{-3}	2.3×10^{-3}
		$\sim 1.5 \times 10^{-3}$	$\sim 4.3 \times 10^{-3}$
	1550	1.8×10^{-7}	3.7×10^{-3}
	1600	2.7×10^{-7}	4.9×10^{-3}
Fe_tO-MgO-SiO_2			
[95Sim][52]	1200	$10^{-10.5}$	$10^{-4.5 \text{ to } -3}$
	1250	$10^{-10.5 \text{ to } -9}$	10^{-3}
[99Nzo][65]	1600	2.0×10^{-7}	7.1×10^{-3}
	1650	4.6×10^{-7}	5.3×10^{-3}
Fe_tO-MnO-SiO_2			
[99Nzo][65]	1400	3.6×10^{-8}	1.5×10^{-3}
	1500	8.2×10^{-8}	4.4×10^{-3}
	1600	2.0×10^{-7}	7.1×10^{-3}
[79Hin][48]	1550	10^{-7}	10^{-5} to 10^{-3}
MnO-Al_2O_3-SiO_2			
[97Nzo1][51]	1550	2.2×10^{-7}	2.8×10^{-3}
	1600	2.0×10^{-7}	6.9×10^{-3}
[65Sha][47]	1650	—	—
CaO-MgO-Al_2O_3-SiO_2			
[98Nzo][58]	1500	8.6×10^{-8}	4.2×10^{-3}
	1600	2.0×10^{-7}	6.9×10^{-3}
	1650	4.6×10^{-7}	5.3×10^{-3}
[60Kal][66]	1500	—	—
[60Abr][40]	1500	—	—
[91Dra][71]	1500	—	—
[99Seo][75]	1500	2.7×10^{-8}	1.4×10^{-2}
[84Kar][72]	1500	—	—
[02One][70]	1400	10^{-11} to 10^{-7}	$10^{-3.5}$
			$\sim 10^{-1.5}$
[03Oht][57]‡	1600	6.9×10^{-11}	—
CaO-MnO-Al_2O_3-SiO_2			
[98Nzo][58]	1500	8.6×10^{-8}	4.2×10^{-3}
	1600	2.0×10^{-7}	6.9×10^{-3}
	1650	4.6×10^{-7}	5.3×10^{-3}
CaO-Fe_tO-MgO-Al_2O_3-SiO_2			
[99Seo][75]	1500	2.7×10^{-8}	1.4×10^{-2}
[02One][70]	1400	10^{-11} to 10^{-7}	$10^{-3.5}$
			$\sim 10^{-1.5}$
CaO-MgO-MnO-Al_2O_3-SiO_2			
[98Nzo][58]	1500	8.6×10^{-8}	4.2×10^{-3}
	1600	2.0×10^{-7}	6.9×10^{-3}
	1650	4.6×10^{-7}	5.3×10^{-3}
CaO-Fe_tO-MgO-MnO-Al_2O_3-SiO_2			
[99Nzo][65]	1550	2.2×10^{-7}	2.8×10^{-3}
	1600	2.0×10^{-7}	6.9×10^{-3}
	1650	4.6×10^{-7}	5.3×10^{-3}
MnO-SiO_2-TiO_x			
[97Ito][49]‡	1400	2.0×10^{-11}	—
CaO-MgO-TiO_x			
[82Bro][42]	1500	10^{-9}	10^{-3}
CaO-SiO_2-TiO_x			
[00Cha][44]	1570	7.0×10^{-9},	—
		5.0×10^{-7}	
[81Bro][63]	1503	—	—
[82Bro][42]	1500	10^{-9},	10^{-3},
		3.9×10^{-14}	6.2×10^{-6}
Fe_tO-SiO_2-TiO_x			
[82Ghi][76]	1500	10^{-9}	1.7×10^{-4}
CaO-MgO-SiO_2-TiO_x			
[82Bro][42]	1500	10^{-9}	10^{-3}
CaO-Al_2O_3-SiO_2-TiO_x			
[82Bro][42]	1500	3.9×10^{-14}	6.2×10^{-6}
CaO-MgO-Al_2O_3-SiO_2-TiO_x			
[02One][70]	1400	$10^{-9.6}$	$10^{-1.9}$

*Fe, MgO cosaturated
**Equilibrium P_{O_2} and P_{S_2} were calculated using FactSage from known experimental input gas composition
†Slag-Ag equilibration.
‡Slag-Cu equilibration.
§Fe, CaO cosaturated.

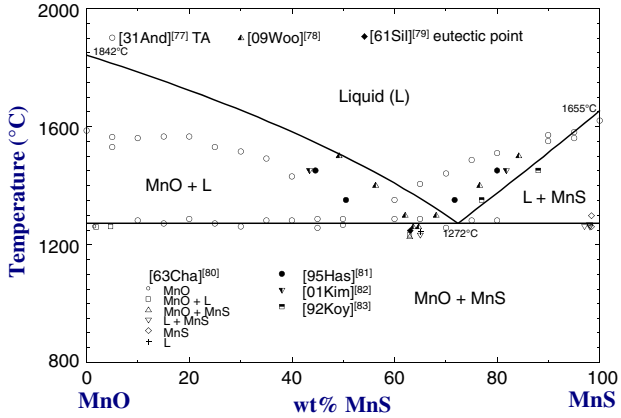

Fig. 36—Calculated MnO-MnS phase diagram compared with experimental data.[77–83]

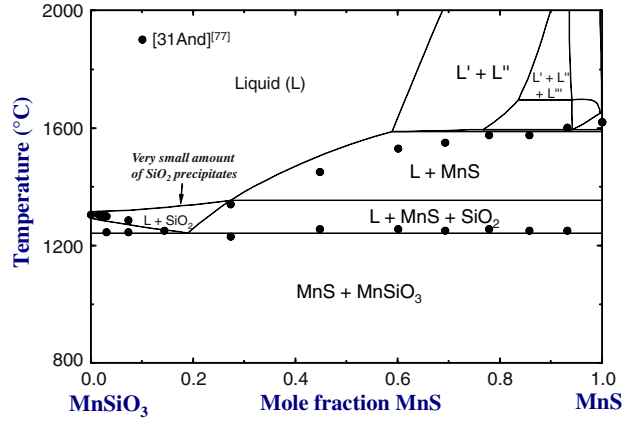

Fig. 38—Calculated phase diagram of the MnO-SiO_2-MnS system along the $MnSiO_3$-MnS join compared with experimental data.[77]

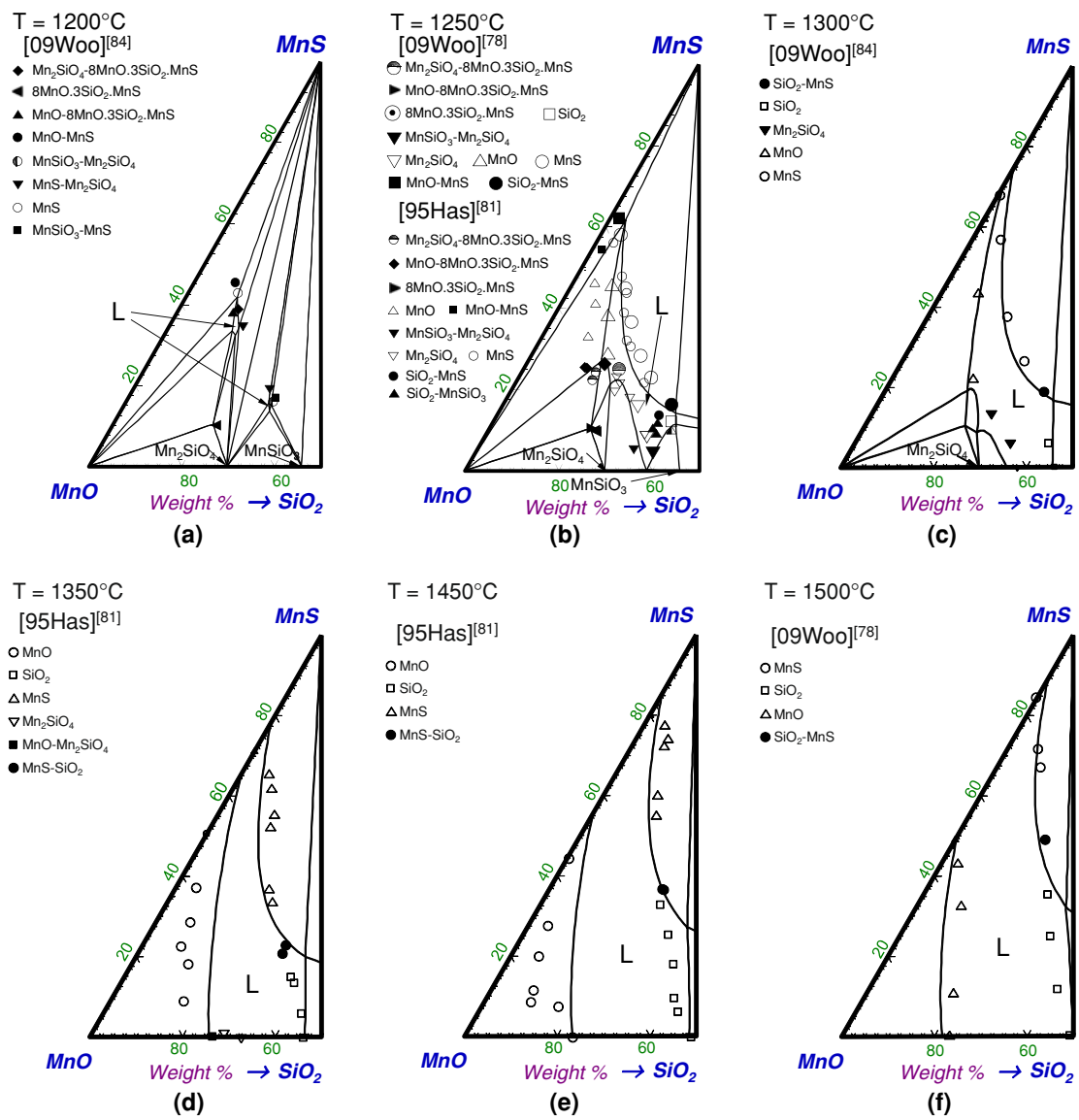

Fig. 37—Calculated phase diagram of the MnO-SiO_2-MnS system compared with experimental data.[78,81,84] Symbols indicate liquidus composition in equilibrium with specified solid phase(s) except for the symbols ▶[81] and ◀,[78,84] which indicate the composition of the ternary compound.

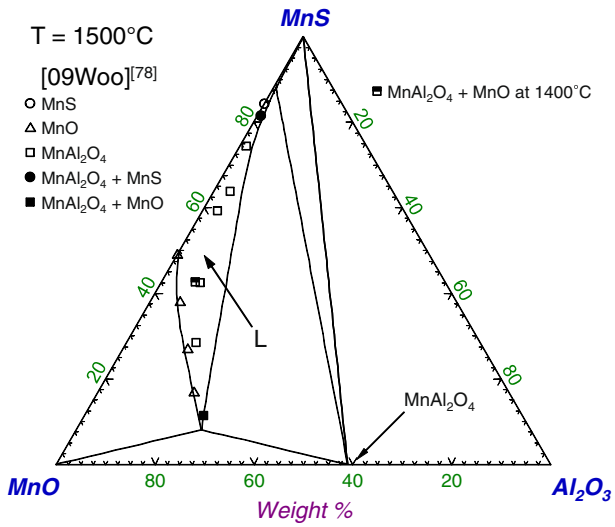

Fig. 39—Calculated phase diagram of the MnO-Al_2O_3-MnS system at 1500 °C compared with experimental data.[78]

parameters were required for any other slag systems, this may be related to the fact that Na_2O is the only oxide of a monovalent cation for which data are available, or it may suggest that the data for Na_2O-containing slags are in error. Experimental problems in measurements that involve alkali-containing slags are well known, particularly at higher alkali contents where the disagreement between the calculated and experimental sulfide capacities is greatest.

VIII. CONCLUSIONS

A general thermodynamic model has been developed to describe the solubility in molten oxide slags of gaseous species such as sulfide, sulfate, nitride, carbide, and water, using the MQM in the quadruplet approximation. This model takes into account FNN and SNN short-range ordering simultaneously. The model takes the activities of the oxide components from the existing evaluated FactSage[8,9] thermodynamic database for oxide slags. Gibbs energies of pure liquid component sulfides are taken from standard compilations. With no additional model parameters, predictions of sulfide capacities, within or nearly within experimental error limits, are obtained with all literature data for Al_2O_3-CaO-FeO-Fe_2O_3-MgO-MnO-SiO_2-TiO_2-Ti_2O_3 slags. The model applies at sulfide contents up to pure liquid sulfide and from highly basic to highly acidic slags.

The database forms part of the FactSage thermodynamic database computing system. By combining this database with other evaluated databases, such as those for molten metal and gaseous phases, and with the general FactSage Gibbs energy minimization software, practically important slag/metal/gas/solid equilibria can be calculated such as S-distribution ratios and gas impurity pick-up levels in molten steel.

ACKNOWLEDGMENTS

This study was supported by a grant from the Fundamental R&D Program for Core Technology of Materials funded by the Ministry of Commerce, Industry and Energy, Republic of Korea. One author (Y.B.K.) would like to thank Mr. D.-H. Woo (POSTECH, Korea) for providing unpublished experimental data.

REFERENCES

1. D.J. Sosinsky and I.D. Sommerville: *Metall. Trans. B*, 1986, vol. 17B, pp. 331–37.
2. M.M. Nzotta, M. Andreasson, P. Jönsson, and S. Seetharaman: *Scand. J. Metall.*, 2000, vol. 29, pp. 177–84.
3. H. Gaye and J. Lehmann: *Proc. 5th Int'l. Conference on Molten Slags, Fluxes and Salts*, ISS, Warrendale, PA, 1997, pp. 27–34.
4. R.G. Reddy and M. Blander: *Metall. Trans. B*, 1987, vol. 18B, pp. 591–96.
5. A.D. Pelton, G. Eriksson, and A. Remero-Serrano: *Metall. Trans. B*, 1993, vol. 24B, pp. 817–25.
6. A.D. Pelton: *Glastech. Ber.*, 1999, vol. 72, pp. 214–26.
7. A.D. Pelton, P. Chartrand, and G. Eriksson: *Metall. Mater. A.*, 2001, vol. 32A, pp. 1409–16.
8. C. Bale, P. Chartrand, S. Degterov, G. Eriksson, K. Hack, R.B. Mahfoud, J. Melançon, A. Pelton, and S. Petersen: *CALPHAD*, 2002, vol. 26, pp. 189–228.
9. C.W. Bale, E. Bélisle, P. Chartrand, S.A. Decterov, G. Eriksson, K. Hack, I.-H. Jung, Y.-B. Kang, J. Melançon, A.D. Pelton, C. Robelin, and S. Petersen: *CALPHAD*, 2009, vol. 33, pp. 295–311.
10. P. Chartrand and A.D. Pelton: *Metall. Mater. Trans. A*, 2001, vol. 32A, pp. 1417–30.
11. P. Chartrand and A.D. Pelton: *Light Metals*, TMS, Warrendale, PA, 2002, pp. 245–52.
12. P. Coursol, A.D. Pelton, P. Chartrand, and M. Zamalloa: *Metall. Mater. Trans. B*, 2005, vol. 36B, pp. 825–36.
13. D. Lindberg, R. Backman, M. Hupa, and P. Chartrand: *J. Chem. Thermodyn.*, 2006, vol. 38, pp. 900–15.
14. G. Eriksson, P. Wu, M. Blander, and A.D. Pelton: *Can. Met. Q.*, 1994, vol. 33, pp. 13–22.
15. P. Wu, G. Eriksson, and A.D. Pelton: *J. Amer. Ceram. Soc.*, 1993, vol. 76, pp. 2065–75.
16. G. Eriksson and A.D. Pelton: *Metall. Trans. B*, 1993, vol. 24B, pp. 807–16.
17. G. Eriksson and A.D. Pelton: *Metall. Trans. B*, 1993, vol. 24B, pp. 795–805.
18. G. Eriksson, P. Wu, and A.D. Pelton: *CALPHAD*, 1993, vol. 17, pp. 189–206.
19. S.A. Decterov, I.-H. Jung, and A.D. Pelton: *J. Am. Ceramic Soc.*, 2002, vol. 85, pp. 2903–10.
20. S.A. Decterov, I.-H. Jung, E. Jak, Y.-B. Kang, P. Hayes, and A.D. Pelton: *Proc. 7th Int'l. Conference on Molten Slags, Fluxes and Salts*, The South African Institute of Mining and Metallurgy, Johannesburg, South Africa, 2004, pp. 839–49.
21. I.-H. Jung, Y.-B Kang, S.A. Decterov, and A.D. Pelton: *Metall. Mater. Trans. B*, 2004, vol. 35B, pp. 259–68.
22. Y.-B. Kang, I.-H Jung, S. Decterov, A.D. Pelton, and H.-G. Lee: *ISIJ Int.*, 2004, vol. 44, pp. 965–74.
23. Y.-B. Kang, I.-H Jung, S. Decterov, A.D. Pelton, and H.-G. Lee: *ISIJ Int.*, 2004, vol. 44, pp. 975–83.
24. I.-H. Jung, S. Decterov, and A.D. Pelton: *J. Phase Equilibria*, 2004, vol. 25, pp. 329–45.
25. I.-H. Jung, S. Decterov, and A.D. Pelton: *J. Phys. Chem. Solids*, 2004, vol. 65, pp. 1683–95.
26. I.-H. Jung, S. Decterov, and A.D. Pelton: *Metall. Mater. Trans. B*, 2004, vol. 35B, pp. 877–89.
27. I.-H. Jung, S. Decterov, and A.D. Pelton: *J. Eur. Ceram. Soc.*, 2005, vol. 25, pp. 313–33.
28. Y.-B. Kang, I.-H. Jung, and H.-G. Lee: *CALPHAD*, 2006, vol. 30, pp. 235–47.

29. Y.-B. Kang, I.-H. Jung, and H.-G. Lee: *CALPHAD*, 2006, vol. 30, pp. 226–34.
30. E. Jak, P. Hayes, A. Pelton, and S.A. Decterov: *Int. J. Mater. Res.*, 2007, vol. 98, pp. 847–54.
31. D.R. Stull and H. Prophet: *JANAF Thermochemical Tables*, U.S. Department of Commerce, Washington, DC, 1985.
32. I. Barin, O. Knacke, and O. Kubaschewski: *Thermochemical Properties of Inorganic Substances*, Springer-Verlag, Berlin, Germany, 1977.
33. A.F. Holleman and E. Wiberg: *Inorganic Chemistry*, Academic Press, San Diego, CA, 2001.
34. P. Waldner and A. Pelton: *J. Phase Equilib. Diffus.*, 2005, vol. 26, pp. 23–38.
35. K.C. Mills: *Thermodynamic Data for Inorganic Sulphides, Selenides and Tellurides*, Butterworths, London, UK, 1974.
36. L.-I. Staffansson: *Metall. Trans. B*, 1976, vol. 7B, pp. 131–34.
37. J.P. Coughlin: *J. Am. Chem. Soc.*, 1950, vol. 72, pp. 5445–47.
38. SGTE pure substance database: http://www.sgte.org, 2007.
39. C.J.B. Fincham and F.D. Richardson: *J. Iron Steel Inst.*, 1954, vol. 178, pp. 4–15.
40. K.P. Abraham, M.W. Davies, and F.D. Richardson: *J. Iron Steel Inst.*, 1960, vol. 196, pp. 309–12.
41. P.T. Carter and T.G. Macfarlane: *J. Iron Steel Inst.*, 1957, vol. 185, pp. 62–66.
42. S.D. Brown, R.J. Roxburgh, I. Ghita, and H.B. Bell: *Ironmak. Steelmak.*, 1982, vol. 9, pp. 163–67.
43. M. Gornerup and O. Wijk: *Scand. J. Metall.*, 1996, vol. 25, pp. 103–07.
44. M. Chapman, O. Ostrovski, G. Tranell, and S. Jahanshahi: *Elektrometallurgiya*, 2000, pp. 34–39.
45. K.P. Abraham and F.D. Richardson: *J. Iron Steel Inst.*, 1960, vol. 196, pp. 313–17.
46. M.M. Nzotta, R. Nilsson, D. Sichen, and S. Seetharaman: *Ironmak. Steelmak.*, 1997, vol. 24, pp. 300–05.
47. R.A. Sharma and F.D. Richardson: *Trans. Met. Soc. AIME*, 1965, vol. 223, pp. 1586–92.
48. M. Hino and T. Fuwa: *Proc. 3rd Int. Iron and Steel Congress*, ASM International, Materials Park, OH, 1979, pp. 321–26.
49. M. Ito, K. Morita, and N. Sano: *ISIJ Int.*, 1997, vol. 37, pp. 839–43.
50. T. Kobayashi, K. Morita, and N. Sano: *Metall. Mater. Trans. B*, 1996, vol. 27B, pp. 652–57.
51. M. Nzotta: *Scand. J. Metall.*, 1997, vol. 26, pp. 169–77.
52. S.R. Simeonov, R. Sridhar, and J.M. Toguri: *Metall. Trans. B*, 1995, vol. 26B, pp. 325–34.
53. E. Drakaliysky, R. Nilsson, D. Sichen, and S. Seetharaman: *High Temp. Mater. Process.*, 1994, vol. 23, pp. 263–72.
54. M. Hino, S. Kitagawa, and S. Ban-Ya: *ISIJ Int.*, 1993, vol. 33, pp. 36–42.
55. G.J.W. Kor and F.D. Richardson: *J. Iron Steel Inst.*, 1968, vol. 206, pp. 700–04.
56. R.A. Sharma and F.D. Richardson: *J. Iron Steel Inst.*, 1961, vol. 198, pp. 386–90.
57. M. Ohta, T. Kubo, and K. Morita: *Tetsu-to-Hagane*, 2003, vol. 89, pp. 742–49.
58. M.M. Nzotta, D. Sichen, and S. Seetharaman: *ISIJ Int.*, 1998, vol. 38, pp. 1170–79.
59. K. Karsrud: *Scand. J. Metall.*, 1984, vol. 13, pp. 173–75.
60. K. Karsrud: *Scand. J. Metall.*, 1984, vol. 13, pp. 265–68.
61. M.M. Nzotta, D. Sichen, and S. Seetharaman: *ISIJ Int.*, 1999, vol. 39, pp. 657–63.
62. J.-D. Shim and S. Ban-Ya: *Tetsu-to-Hagane*, 1982, vol. 68, pp. 251–60.
63. A. Bronson and G.R. St Pierre: *Metall. Trans. B.*, 1981, vol. 12B, pp. 729–31.
64. M.M. Nzotta: *High Temp. Mater. Process.*, 1997, vol. 16, pp. 261–71.
65. M.M. Nzotta, D. Sichen, and S. Seetharaman: *Metall. Trans. B.*, 1999, vol. 30B, pp. 909–20.
66. M.R. Kalyanram, T.G. Macfarlane, and H.B. Bell: *J. Iron Steel Inst.*, 1960, vol. 195, pp. 58–64.
67. R. Nilsson and S. Seetharaman: *Scand. J. Metall.*, 1995, vol. 24, pp. 81–86.
68. S. Ban-Ya, M. Hino, A. Sato, and O. Terayama: *Tetsu-to-Hagane*, 1991, vol. 77, pp. 361–68.
69. Y. Taniguchi, N. Sano, and S. Seetharaman: *Proc. Sano Symposium*, Inst. Industrial Science, University of Tokyo, Tokyo, Japan, 2008, pp. 145–51.
70. H.St.C. O'Neill and J.A. Mavrogenes: *J. Petrol.*, 2002, vol. 43, pp. 1049–87.
71. E. Drakaliysky, N.S. Srinivasan, and L.-I. Staffansson: *Scand. J. Metall.*, 1991, vol. 20, pp. 251–55.
72. K. Karsrud: *Scand. J. Metall.*, 1984, vol. 13, pp. 144–50.
73. E. Drakaliysky, D. Sichen, and S. Seetharaman: *Can. Metall. Q.*, 1997, vol. 36, pp. 115–20.
74. J. Cameron, T.B. Gibbons, and J. Taylor: *J. Iron Steel Inst.*, 1966, vol. 206, pp. 1223–28.
75. J.-D. Seo and S.-H. Kim: *Steel Res.*, 1999, vol. 70, pp. 203–08.
76. I. Ghita and H.B. Bell: *Ironmak. Steelmak.*, 1982, vol. 9, pp. 239–43.
77. J.H. Andrew, W.R. Maddocks, and E.A. Fowler: *J. Iron Steel Inst.*, 1931, vol. 124, pp. 295–325.
78. D.-H. Woo, Y.-B. Kang, H. Gaye, and H.-G. Lee: *Proc. 8th Int'l. Conference on Molten Slags, Fluxes and Salts*, Universidad de Concepción, Concepción Province, Chile, 2009, pp. 143–48.
79. E.N. Silverman: *Trans. Met. Soc. AIME*, 1961, vol. 221, pp. 512–17.
80. H.C. Chao, Y.E. Smith, and L.H. Van Vlack: *Trans. Met. Soc. AIME*, 1963, vol. 227, pp. 796–97.
81. A. Hasegawa, K. Morita, and N. Sano: *Tetsu-to-Hagane*, 1995, vol. 81, pp. 1109–13.
82. T.-G. Kim, W.-K. Lee, J.-H. Park, D.-J. Min, and H.-S. Song: *ISIJ Int.*, 2002, vol. 41, pp. 1460–64.
83. N. Koyama, F. Tsukihashi, and N. Sano: *Tetsu-to-Hagane*, 1993, vol. 79, pp. 1334–37.
84. D.-H. Woo: unpublished research, GIFT, POSTECH, Pohang, Korea, 2009.